Published in final edited form as:
Arterioscler Thromb Vasc Biol. 2015 January ; 35(1): 189–196. doi:10.1161/ATVBAHA.114.304483.

In Vivo Nanoparticle Assessment of Pathological Endothelium Predicts the Development of Inflow Stenosis in Murine Arteriovenous Fistula

Jie Cui, M.D.[*,1,2], **Chase W. Kessinger, Ph.D.**[*,1], **Jason R. McCarthy, Ph.D.**[3], **David E. Sosnovik, M.D.**[1,4], **Peter Libby, M.D.**[5], **Ravi I. Thadhani, M.D., M.P.H.**[2], and **Farouc A. Jaffer, M.D., Ph.D.**[1,6]

[1]Cardiovascular Research Center, Division of Cardiology, Massachusetts General Hospital, Harvard Medical School, Boston, Massachusetts

[2]Nephrology Division, Massachusetts General Hospital, Harvard Medical School, Boston, Massachusetts

[3]Center for System Biology, Massachusetts General Hospital, Harvard Medical School, Boston, Massachusetts

[4]Martinos Center for Biomedical Imaging, Massachusetts General Hospital, Harvard Medical School, Boston, Massachusetts

[5]Cardiology Division, Brigham and Women's Hospital, Harvard Medical School, Boston, Massachusetts

[6]Wellman Center for Photomedicine, Massachusetts General Hospital, Harvard Medical School, Boston, Massachusetts

Abstract

Objective—*In vivo* assessment of pathological endothelium within arteriovenous fistula (AVF) could provide new insights into inflow stenosis, a common cause of AVF primary failure in end stage renal disease patients. Here we developed nanoparticle-based imaging strategies to assess pathological endothelium *in vivo*, and elucidate its relationship to neointimal hyperplasia formation in AVF.

Approach and Results—Jugular-carotid AVFs were created in C57BL/6 mice (n=38). Pathological endothelium in the AVF was visualized and quantified *in vivo* using dextranated magnetofluorescent nanoparticles (CLIO-VT680). At day 14, CLIO-VT680 deposited in AVF, but only minimally in sham-operated arteries. Transmission electron microscopy revealed that CLIO-VT680 resided within endothelial cells and in the intimal extracellular space. Endothelial cells of AVF, but not control arteries, expressed VCAM-1, and showed augmented endothelial permeability near the anastomosis. Intravital microscopy (IVM) demonstrated that CLIO-VT680

Correspondence: Farouc A. Jaffer, MD PhD, MGH CVRC, Simches Research Building, Room 3206, 185 Cambridge Street, Boston, Massachusetts 02114, fjaffer@mgh.harvard.edu, Tel. (617) 724-9353, Fax. (617) 860-3180.
[*]JC and CWK contributed equally

Disclosures
None of the authors declared competing interests.

deposited most intensely near the AVF anastomosis ($p < 0.0001$). The day 14 IVM CLIO-VT680 signal predicted the subsequent site and magnitude of AVF neointimal hyperplasia at day 42 ($r=0.58$, $p < 0.05$). CLIO-VT680 deposition in AVF was further visualized by *ex vivo* MRI.

Conclusions—AVF develop a pathological endothelial response that can be assessed *in vivo* via nanoparticle-enhanced imaging. AVF endothelium is activated and exhibits augmented permeability, offering a targeting mechanism for nanoparticle deposition and retention in pathological endothelium. The *in vivo* AVF nanoparticle signal identified and predicted subsequent inflow neointimal hyperplasia. This approach could be used to test therapeutic interventions aiming to restore endothelial health and to decrease early AVF failure caused by inflow stenosis.

Keywords

arteriovenous fistula; endothelium; neointimal hyperplasia; stenosis; nanoparticle; imaging

INTRODUCTION

Hemodialysis is a life-sustaining treatment for 1.5 million end-stage renal disease patients across the world.[1] Effective hemodialysis treatment requires reliable large caliber vascular access. Dysfunctional dialysis access disrupts scheduled dialysis treatment, and associates with higher mortality rates.[2–4] Thus preservation of patent dialysis access is essential to the care of hemodialysis patients. Arteriovenous fistulae (AVFs), the preferred access route for hemodialysis, have an unacceptably high failure rate.[5] After surgical creation, up to 30–50% of AVFs are unsuitable for hemodialysis due to a failure to mature. In contrast to late AVF failures, which are usually caused by thrombosis and venous neointimal hyperplasia, early AVF failures primarily result from juxta-anastomotic inflow stenosis.[6]

Pathologically altered endothelium is implicated in AVF failure.[7–9] At present however there is minimal understanding of the role of pathological endothelium in AVF failure *in vivo*. The ability to assess AVF endothelium *in vivo* could furnish new insights into the topography of pathological endothelium, and its site-specific relationship to the subsequent development of inflow stenosis, a common cause of AVF failure.

This study tested the hypothesis that fluorescence and MRI imaging of dextran-coated nanoparticle deposition could assess dysfunctional endothelium within AVF. After demonstrating anastomosis-based nanoparticle uptake by AVF, but not sham-operated control vessels, this study explored mechanisms underlying nanoparticle retention in AVF. We further tested the hypothesis that the intensity and location of the pathological endothelial signal on AVF imaging would predict the subsequent extent and location of neointimal hyperplasia within the maturing AVF.

MATERIAL AND METHODS

A study flowchart (Supplemental Figure I), and detailed methods are available in the Online supplement.

RESULTS

Measurement of blood flow following AVF creation

Murine AVF were created using an established common carotid artery-jugular vein end-to-side anastomosis approach (Supplemental Figure IIA).[10–13] The anastomosis was defined as the surgical connection between the carotid artery and the jugular vein. AVFs exhibited a 7-fold increase in carotid arterial blood flow compared to baseline (pre: 0.35 ±0.03 mL/min versus post: 2.56 ± 0.28 mL/min; $p < 0.0001$, Supplemental Figure IIB). Mice that developed acute venous thrombosis immediately after AVF creation were excluded from further study (n=9 of 47, blood flow < 0.1 mL/min).

Histological assessment of inflow neointimal hyperplasia in murine AVF

To examine whether these experimental AVFs could recapitulate human inflow AVF stenosis, a group of mice were sacrificed 42 days after AVF surgery (n=7). Modified Verhoeff Van Gieson histological stain visualized elastin layers within the AVF. Neointimal hyperplasia was evident in the juxta-anastomotic arterial limb. The area of neointimal hyperplasia, calculated as the area between the lumen and the internal elastic lamina, steadily decreased with increasing distance away from the anastomosis ($r=-0.89$; $p=0.0067$; Figure 1). Sham-operated contralateral vessels did not develop neointimal hyperplasia.

CLIO-VT680 nanoparticles report on pathological endothelium in AVF

To assess the *in vivo* vascular endothelial response after AVF creation, dextranated magnetofluorescent nanoparticles (CLIO-VT680, 10 mg Fe/kg) were intravenously injected into day 14 post-AVF surgery mice (n=9). CLIO-VT680 nanoparticles have a hydrodynamic diameter of 49 nm with a 5 nm iron oxide core, and can be phagocytosed by murine macrophages, endothelial cells, and smooth muscle cells in vascular disease states.[14, 15] After 24 hours, mice receiving CLIO-VT680 were sacrificed and AVF were resected. Fluorescence microscopy (FM) revealed that CLIO-VT680 nanoparticles deposited in the juxta-anastomotic arterial segment of the AVF, but minimally in contralateral sham-operated vessels (Figure 2A). CLIO-VT680 mainly colocalized with CD31-positive endothelial cells. Minute areas of nanoparticle deposition were also evident in the smooth muscle cell-rich superficial medial layer (Figure 2A). Endothelial cells of AVF, but not sham-operated arteries, expressed vascular cell adhesion molecule-1 (VCAM)-1, a marker of endothelial cell activation (Figure 2B).[16] *En face* confocal analysis of the AVF segment also demonstrated CLIO-VT680 deposition near the anastomosis (Figure 2C).

Transmission electron microscopy (TEM) of AVF tissue sections sampled at day 14 revealed the precise localization of the nanoparticles within AVF (Figure 3A). The electron dense iron oxide core (5 nm) of the CLIO-VT680 nanoparticles were identified as hypointense signal areas on TEM, and localized inside endothelial cells, as well as in the subendothelial intimal space bordered by the internal elastic lamina. Sham-operated control arteries showed minimal nanoparticle deposition.

As the TEM images revealed subendothelial deposition of CLIO-VT680 nanoparticles in AVFs, we hypothesized that AVF would exhibit abnormal endothelial barrier function. To

test this hypothesis, Evans blue was intravenously injected in day 14 animals (n=3), 30 minutes before sacrifice to access endothelial permeability.[17] Light microscopy revealed Evans blue deposition in the juxta-anastomostic area of the AVF, indicating increased permeability. Sham-operated contralateral arteries showed minimal Evans blue staining. Fluorescence reflectance imaging and fluorescence microscopy of Evans blue fluorescence similarly revealed augmented signal in the juxta-anastomotic region of the AVF compared to sham-operated arteries (Figure 3B).

In vivo assessment of pathological endothelium in AVF by intravital fluorescence microscopy

Intravital microscopy (IVM) simultaneously illuminates the molecular and structural details of vascular disease at high resolution *in vivo*.[18] To determine whether nanoparticle-delineated pathological endothelium in AVF could be imaged *in vivo*, mice underwent confocal IVM at day 14 (n=9) and day 21 (n=4) post-AVF surgery, twenty-four hours after CLIO-VT680 administration. AVFs were surgically exposed to allow IVM biological-structural imaging of the anastomosis and the adjacent arterial segment. Areas of pathological endothelium displayed near-infrared fluorescence emission from CLIO-VT680. The vessel wall and lumen were detected and identified jointly by second harmonic generation and fluorescein isothiocyanate-dextran signals, respectively (Supplemental Figure III).[19] IVM coronal Z-stacks were obtained and regions-of-interest (ROIs) were defined as CLIO-VT680 positive areas inside the vessel wall on re-sliced axial micrographs (Figure 4A). The anastomosis was identified by the presence of the AVF sutures. The inability of light to penetrate the nylon sutures precluded analysis of NIRF signals at the site of proximal anastomosis (distance=0 μm).

Analysis of the day 14 IVM data revealed that the highest nanoparticle signal occurred in the juxta-anastomosis arterial segment (Figure 4A). *In vivo* CLIO-VT680 signals decreased linearly as the distance away from the anastomosis increased ($r=-0.98$; $p < 0.0001$, Figure 4C). A similar trend was evident in day 21 AVF ($r=-0.98$; $p < 0.001$, Figure 4C), with higher CLIO-VT680 TBRs compared to day 14 AVF, indicating progressive endothelial abnormality in developing AVF. Utilizing the AVF anastomosis as a fiducial marker, matched *ex vivo* arterial sections similarly demonstrated that day 14 pathological endothelial signal (higher nanoparticle TBR) diminished steadily as the distance from the anastomosis increased ($r=-0.96$, $p < 0.0001$; Figure 4B and 4D). *In vivo* and *ex vivo* nanoparticle TBRs correlated on matched sections ($r=0.59$, $p < 0.0001$, Figure 4E).

Nanoparticle fluorescence in pathological endothelium of AVF predicts the development of arterial neointimal hyperplasia formation

Ex vivo studies link impaired endothelial function to neointimal hyperplasia (NH) and AVF failure.[9, 11] It remains unknown, however, whether imaging of pathological endothelium can quantitatively predict sites of future inflow stenosis. We therefore performed survival IVM imaging of the AVF arterial circuit in day 14 AVF utilizing CLIO-VT680 (n=3), followed by NH assessment at day 42. On day 42, mice were sacrificed and the arterial NH was measured using Verhoeff Van Gieson staining. Anastomosis sutures were used as the 0 μm reference point to match day 14 IVM and day 42 histology (Figure 5A and 5B). Utilizing the

AVF anastomosis as a fiducial marker, we found that both the day 14 *in vivo* CLIO-VT680 signal and day 42 neointimal hyperplasia area steadily decreased with the distance from the anastomosis (n=3 mice, r=−0.98, p=0.0009; r=−0.92, p=0.0089; Figure 5C). The individual day 14 CLIO-VT680 TBR values (reflecting the degree of pathological endothelium) predicted the site and magnitude of NH on day 42 (r=0.58, p=0.016; Figure 5D). A similar correlation was found in an additional group of mice (n=2) utilizing a different batch of CLIO-VT680 (r=0.67, p=0.01, data not shown). The pattern of day 42 neointimal hyperplasia distribution was similar to the day 14 CLIO signal distribution (Supplemental Figure IV).

MRI of pathological endothelium in AVF

To determine whether a clinical imaging modality could assess pathological endothelial function in AVF, *ex vivo* MRI was performed on resected day 14 AVF (n=5). Day 14 mice received CLIO-VT680 nanoparticles or PBS before sacrifice and tissue resection. CLIO-VT680 nanoparticles are derived from ultrasmall superparamagnetic iron oxide (USPIO) nanoparticles that can induce signal loss in T2-weighted magnetic resonance images.[14] In mice that received the magnetofluorescent CLIO-VT680 nanoparticles, strong near-infrared fluorescence (NIRF) signal emanated from the juxta-anastomotic region (arrow head, Figure 6A), consistent with the *in vivo* IVM results. Minimal NIRF signal enhancement occurred in PBS-injected mice. T_2-weighted rapid acquisition with refocused echoes (RARE) images demonstrated signal hypointensity around the AVF anastomosis in CLIO-VT680 injected mice, consistent with the IVM and FRI data. Iron oxide deposition in the arterial AVF segment generated lower MRI signal on T2-weighted images compared to the PBS group (Signal-to-noise ratio: 41.5±1.8, CLIO; vs. 64.9±1.8 PBS, p=0.003; Figure 6B).

DISCUSSION

This study reports the development of a novel nanoparticle-based imaging approach to map and quantify murine AVF-induced pathological endothelial function *in vivo*. It showed that in the early stage, the *in vivo* AVF endothelial injury response predicted the development of later stage AVF arterial neointimal hyperplasia and inflow stenosis. The greatest degree of endothelial injury and neointimal hyperplasia occurred in the juxta-anastomotic arterial segment of the AVF.

Endothelial cells near the AVF anastomosis exhibited greater retention of CLIO nanoparticles, and showed increased permeability and VCAM-1 expression. After AVF creation in humans, arterial blood flow usually increases 40-fold to 1000 ml/min.[20] The response to augmented blood flow as well to the initial surgical procedure can induce endothelial dysfunction, characterized by an imbalance between endothelium-derived vasodilators and vasoconstrictors, abnormal leukocyte-endothelial interactions, and an increased expression of adhesion molecules, as well as impaired vascular integrity and increased permeability.[21, 22] Indeed, we found heightened VCAM-1 expression and Evans blue-delineated endothelial permeability near the AVF anastomosis (Figure 3B), the area that ultimately developed the greatest degree of neointimal hyperplasia and stenosis. Augmented endothelial cell activation and endothelial permeability in AVF further provide

mechanisms for the deposition of CLIO-VT680 nanoparticles in endothelial cells and the subendothelial space, respectively, as revealed by transmission electron microscopy (Figure 3A). Although SMCs within atheroma may phagocytose CLIO nanoparticles,[14] we found little nanoparticle deposition in SMCs within AVF. This observation might relate to differential phagocytic profiles of SMCs in differing arterial disease states,[23] as well as reduced access of CLIO nanoparticles to the deeper medial layers.

While many studies have elucidated mechanisms underlying late AVF failure, such as venous neointimal hyperplasia (NH) and thrombosis, only a few studies have studied *in vivo* mechanisms underlying primary AVF failure, a major clinical problem. The primary failure rate of AVF reaches 30–50%.[24, 25] Inflow stenosis as a subset of juxta-anastomotic stenosis accounts up to one-third of AVF cases referred to interventional centers.[26–28] At present, scant data shed light on *in vivo* biological mechanisms underlying inflow stenosis. This study provides new knowledge into the relationship between *in vivo* regional AVF-related endothelial injury and subsequent inflow neointimal formation. We found that the degree and location of pathological endothelium could predict the development of neointimal hyperplasia at a later stage. The validated experimental methodology here provides a new approach to investigate genetic or pharmacological manipulations of endothelial function *in vivo*, and to assess its subsequent effects on the development of neointimal hyperplasia and inflow stenosis in AVF. In addition, future studies can also investigate the possible contributions of comorbidities relevant to renal patients, such as hyperlipidemia, diabetes and hypertension to mechanisms of AVF failure.

The most commonly utilized clinical imaging method to assess AVF patency is duplex ultrasound. [29] Multidetector computed tomography (MDCT) is another noninvasive tool that can evaluate the entire AVF circuit.[30] X-ray angiography provides structural information and guides AVF treatment, but is invasive. Additional limitations of CT and invasive angiography include the inability to image the biological processes underlying AVF failure, as well as radiation exposure and the risk of contrast-induced nephropathy. Furthermore, none of the current AVF imaging methods accurately predicts inflow stenosis, nor leads to improved AVF patency rates.[31–33] In this study, the initial results with MRI of iron oxide nanoparticle deposition illustrate a possible path to image pathological endothelium in AVF in humans. Clinical magnetic nanoparticles such as ferumoxytol are similar to the CLIO-VT680 nanoparticles employed here, and also induce MRI signal loss on T_2-weighted images.[34] While our feasibility study was limited to *ex vivo* MRI at high-field strength in mice, the larger size and more superficial location of arm AVFs in human subjects might enable noninvasive ferumoxytol-enhanced MRI of pathological endothelial function. New *in vivo* imaging strategies that can identify AVFs at risk for inflow stenosis offer the opportunity to decrease the early fistula failure rate and improve dialysis patients' outcomes. Such high-risk patients might be candidates for surgical AVF revision, endovascular treatment, or for novel pro-endothelial healing approaches to reduce AVF failure.

This study has limitations. While the employed murine AVF approach of carotid artery mobilization differs from the clinical practice of vein mobilization, this murine model is well established experimentally and recapitulates many of the features of human AVF, including inflow stenosis.[10–13] Venous side juxta-anastomotic stenosis, another common

cause of AVF failure, could not be imaged *in vivo* in this study due to limited light penetration through surgery-induced scar tissue. In this first proof-of-concept study, AVF function was investigated in normal mice without uremia. Evaluation of the AVF endothelial injury response in uremic mice will be of substantial interest in future investigations. Confocal IVM has limited depth sensing of up to 200 μm, restricting *in vivo* insights into AVF to the top arc of murine AVF. In contrast, *ex vivo* fluorescence microscopy can image the full depth of the fluorescence signals in the vessel, which may explain a moderate rather than strong correlation between *in vivo* and *ex vivo* CLIO-VT680 signal intensities. Multiphoton IVM approaches may allow deeper high-resolution imaging and could help address this issue, and also allow venous circuit imaging. While this study did not probe directly possible mechanisms of modified endothelial function, altered endothelial shear stress influenced by AVF geometry could contribute to the development of dysfunctional endothelium following AVF creation.[35, 36]

In conclusion, pathological endothelium in murine AVF can be assayed *in vivo* by fluorescence and magnetic resonance imaging of dextranated nanoparticle deposition. The extent and location of abnormal AVF endothelium predicted the local degree of neointimal hyperplasia formation. Such imaging approaches offer the ability to predict the likelihood and even the specific location of inflow stenosis, and further provide a theranostic framework to assess therapies aiming to restore endothelial health and reduce primary AVF failure.

Supplementary Material

Refer to Web version on PubMed Central for supplementary material.

Acknowledgements

The authors thank Dr. Charles P. Lin for his expertise and assistance with intravital microscopy. The authors also thank Dr. Amin Arnaout and Dr. Joseph Bonventre for project advice, Dr. Howard H. Chen for MRI expertise, and Dr. James McDaid for assistance with vascular surgery. The authors acknowledge Gregory Wojtkiewicz, M.S., Dr. Matthias Nahrendorf, and Dr. Ralph Weissleder for assistance with MRI imaging, and Mary McKee for TEM assistance. Electron microscopy was performed in the Microscopy Core of the Center for Systems Biology/Program in Membrane Biology, which is partially supported by an Inflammatory Bowel Disease Grant DK43351 and a Boston Area Diabetes and Endocrinology Research Center (BADERC) Award DK57521. An abstract of this report was presented at the Arteriosclerosis, Thrombosis and Vascular Biology 2013 scientific sessions and the World Molecular Imaging Congress 2013 sessions.

Sources of funding:

This study was supported by grants from the American Society of Nephrology Ben J. Lipps Research Fellowship (to J.C.), National Institutes of Health (NIH) R01 HL108229 (F.A.J.), R01 HL080472 (P. L.), American Heart Association Grant-in-Aid #13GRNT17060040 (F.A.J.), NIH T32 HL076136 (C.W.K), NIH P41 E8015903-02S1 (C.P.L.) and the Nephrology Division at Massachusetts General Hospital.

Nonstandard Abbreviations and Acronyms

AVF	arteriovenous fistula
CLIO-VT680	cross-linked iron oxide-VivoTag680
IVM	intravital microscopy

MRI	magnetic resonance imaging
NH	neointimal hyperplasia
TBR	target-to-background ratio
VCAM-1	vascular cell adhesion molecule-1

References

1. Collins AJ, Foley RN, Herzog C, et al. US renal data system 2012 annual data report. Am J Kidney Dis. 2013; 61(A7):e1–e476.
2. Feldman HI, Held PJ, Hutchinson JT, Stoiber E, Hartigan MF, Berlin JA. Hemodialysis vascular access morbidity in the United States. Kidney Int. 1993; 43:1091–1096. [PubMed: 8510387]
3. Feldman HI, Kobrin S, Wasserstein A. Hemodialysis vascular access morbidity. J Am Soc Nephrol. 1996; 7:523–535. [PubMed: 8724885]
4. Foley RN, Gilbertson DT, Murray T, Collins AJ. Long interdialytic interval and mortality among patients receiving hemodialysis. N Engl J Med. 2011; 365:1099–1107. [PubMed: 21992122]
5. Gold JA, Hoffman K. Fistula first: The national vascular access improvement initiative. WMJ. 2006; 105:71–73. [PubMed: 16749331]
6. Roy-Chaudhury P, Sukhatme VP, Cheung AK. Hemodialysis vascular access dysfunction: A cellular and molecular viewpoint. J Am Soc Nephrol. 2006; 17:1112–1127. [PubMed: 16565259]
7. Juncos JP, Tracz MJ, Croatt AJ, Grande JP, Ackerman AW, Katusic ZS, Nath KA. Genetic deficiency of heme oxygenase-1 impairs functionality and form of an arteriovenous fistula in the mouse. Kidney Int. 2008; 74:47–51. [PubMed: 18368029]
8. Liang A, Wang Y, Han G, Truong L, Cheng J. Chronic kidney disease accelerates endothelial barrier dysfunction in a mouse model of an arteriovenous fistula. Am J Physiol Renal Physiol. 2013; 304:F1413–F1420. [PubMed: 23576636]
9. Wang Y, Liang A, Luo J, Liang M, Han G, Mitch WE, Cheng J. Blocking notch in endothelial cells prevents arteriovenous fistula failure despite CKD. J Am Soc Nephrol. 2014; 25:773–783. [PubMed: 24480830]
10. Castier Y, Lehoux S, Hu Y, Foteinos G, Tedgui A, Xu Q. Characterization of neointima lesions associated with arteriovenous fistulas in a mouse model. Kidney Int. 2006; 70:315–320. [PubMed: 16760906]
11. Feng W, Chumley P, Allon M, George J, Scott DW, Patel RP, Litovsky S, Jaimes EA. The transcription factor E26 transformation-specific sequence-1 mediates neointima formation in arteriovenous fistula. J Am Soc Nephrol. 2014; 25:475–487. [PubMed: 24203999]
12. Juncos JP, Grande JP, Kang L, Ackerman AW, Croatt AJ, Katusic ZS, Nath KA. MCP-1 contributes to arteriovenous fistula failure. J Am Soc Nephrol. 2011; 22:43–48. [PubMed: 21115617]
13. Kokubo T, Ishikawa N, Uchida H, Chasnoff SE, Xie X, Mathew S, Hruska KA, Choi ET. CKD accelerates development of neointimal hyperplasia in arteriovenous fistulas. J Am Soc Nephrol. 2009; 20:1236–1245. [PubMed: 19423694]
14. Jaffer FA, Nahrendorf M, Sosnovik D, Kelly KA, Aikawa E, Weissleder R. Cellular imaging of inflammation in atherosclerosis using magnetofluorescent nanomaterials. Mol Imaging. 2006; 5:85–92. [PubMed: 16954022]
15. Ripplinger CM, Kessinger CW, Li C, Kim JW, McCarthy JR, Weissleder R, Henke PK, Lin CP, Jaffer FA. Inflammation modulates murine venous thrombosis resolution in vivo: Assessment by multimodal fluorescence molecular imaging. Arterioscler Thromb Vasc Biol. 2012; 32:2616–2624. [PubMed: 22995524]
16. Cybulsky MI, Gimbrone MA Jr. Endothelial expression of a mononuclear leukocyte adhesion molecule during atherogenesis. Science. 1991; 251:788–791. [PubMed: 1990440]

17. Stehbens WE. Endothelial permeability in experimental aneurysms and arteriovenous fistulas in rabbits as demonstrated by the uptake of evans blue. Atherosclerosis. 1978; 30:343–349. [PubMed: 708491]
18. Taqueti VR, Jaffer FA. High-resolution molecular imaging via intravital microscopy: Illuminating vascular biology in vivo. Integr Biol (Camb). 2013; 5:278–290. [PubMed: 23135362]
19. Saxena A, Kessinger CW, Thompson B, McCarthy JR, Iwamoto Y, Lin CP, Jaffer FA. High-resolution optical mapping of inflammatory macrophages following endovascular arterial injury. Mol Imaging Biol. 2013; 15:282–289. [PubMed: 23090852]
20. Joannides R, Haefeli WE, Linder L, Richard V, Bakkali EH, Thuillez C, Luscher TF. Nitric oxide is responsible for flow-dependent dilatation of human peripheral conduit arteries in vivo. Circulation. 1995; 91:1314–1319. [PubMed: 7867167]
21. Eslami MH, Gangadharan SP, Belkin M, Donaldson MC, Whittemore AD, Conte MS. Monocyte adhesion to human vein grafts: A marker for occult intraoperative injury? J Vasc Surg. 2001; 34:923–929. [PubMed: 11700496]
22. Kipshidze N, Dangas G, Tsapenko M, Moses J, Leon MB, Kutryk M, Serruys P. Role of the endothelium in modulating neointimal formation: Vasculoprotective approaches to attenuate restenosis after percutaneous coronary interventions. J Am Coll Cardiol. 2004; 44:733–739. [PubMed: 15312851]
23. Marx SO, Totary-Jain H, Marks AR. Vascular smooth muscle cell proliferation in restenosis. Circ Cardiovasc Interv. 2011; 4:104–111. [PubMed: 21325199]
24. Huijbregts HJ, Bots ML, Wittens CH, Schrama YC, Moll FL, Blankestijn PJ, group Cs. Hemodialysis arteriovenous fistula patency revisited: Results of a prospective, multicenter initiative. Clin J Am Soc Nephrol. 2008; 3:714–719. [PubMed: 18256379]
25. Dixon BS, Novak L, Fangman J. Hemodialysis vascular access survival: Upper-arm native arteriovenous fistula. Am J Kidney Dis. 2002; 39:92–101. [PubMed: 11774107]
26. Asif A, Gadalean FN, Merrill D, Cherla G, Cipleu CD, Epstein DL, Roth D. Inflow stenosis in arteriovenous fistulas and grafts: A multicenter, prospective study. Kidney Int. 2005; 67:1986–1992. [PubMed: 15840048]
27. Beathard GA, Arnold P, Jackson J, Litchfield T. Physician Operators Forum of RMSL. Aggressive treatment of early fistula failure. Kidney Int. 2003; 64:1487–1494. [PubMed: 12969170]
28. Khan FA, Vesely TM. Arterial problems associated with dysfunctional hemodialysis grafts: Evaluation of patients at high risk for arterial disease. J Vasc Interv Radiol. 2002; 13:1109–1114. [PubMed: 12427810]
29. Wiese P, Nonnast-Daniel B. Colour doppler ultrasound in dialysis access. Nephrol Dial Transplant. 2004; 19:1956–1963. [PubMed: 15199165]
30. Chen MC, Tsai WL, Tsai IC, Chan SW, Liao WC, Lin PC, Yang SJ. Arteriovenous fistula and graft evaluation in hemodialysis patients using MDCT: A primer. AJR Am J Roentgenol. 2010; 194:838–847. [PubMed: 20173168]
31. Tonelli M, James M, Wiebe N, Jindal K, Hemmelgarn B. Alberta Kidney Disease N. Ultrasound monitoring to detect access stenosis in hemodialysis patients: A systematic review. Am J Kidney Dis. 2008; 51:630–640. [PubMed: 18371539]
32. Plantinga LC, Jaar BG, Astor B, Fink NE, Eustace JA, Klag MJ, Powe NR. Association of clinic vascular access monitoring practices with clinical outcomes in hemodialysis patients. Nephron Clin Pract. 2006; 104:c151–c159. [PubMed: 16902311]
33. Polkinghorne KR, Lau KK, Saunder A, Atkins RC, Kerr PG. Does monthly native arteriovenous fistula blood-flow surveillance detect significant stenosis--a randomized controlled trial. Nephrol Dial Transplant. 2006; 21:2498–2506. [PubMed: 16854848]
34. Alam SR, Shah AS, Richards J, Lang NN, Barnes G, Joshi N, MacGillivray T, McKillop G, Mirsadraee S, Payne J, Fox KA, Henriksen P, Newby DE, Semple SI. Ultrasmall superparamagnetic particles of iron oxide in patients with acute myocardial infarction: Early clinical experience. Circ Cardiovasc Imaging. 2012; 5:559–565. [PubMed: 22875883]
35. Nagel T, Resnick N, Atkinson WJ, Dewey CF Jr. Gimbrone MA Jr. Shear stress selectively upregulates intercellular adhesion molecule-1 expression in cultured human vascular endothelial cells. J Clin Invest. 1994; 94:885–891. [PubMed: 7518844]

36. Krams R, Wentzel JJ, Oomen JA, Vinke R, Schuurbiers JC, de Feyter PJ, Serruys PW, Slager CJ. Evaluation of endothelial shear stress and 3D geometry as factors determining the development of atherosclerosis and remodeling in human coronary arteries in vivo. Combining 3D reconstruction from angiography and IVUS (ANGUS) with computational fluid dynamics. Arterioscler Thromb Vasc Biol. 1997; 17:2061–2065. [PubMed: 9351372]

Significance

Arteriovenous fistulae (AVFs) or grafts are the “lifelines” for 1.5 million end stage renal disease patients receiving dialysis. Dysfunctional vascular access disrupts dialysis treatment and is associated with higher mortality rates. Notably the primary failure rate of AVF reaches 30–50%, and current clinical modalities do not accurately predict access failure. Hence we developed nanoparticle-based fluorescence and MRI imaging approaches to image pathological endothelium, a key driver of AVF failure. We found that the intensity of nanoparticle deposition visualized the degree of endothelial pathology, and was highest at the AVF anastomosis. Nanoparticle deposition further predicted the development of local neointimal formation and inflow stenosis within maturing AVF. The overall results provide a framework to assess genetic and pharmacological manipulations of endothelial biology and their *in vivo* effects of neointimal formation in AVF. Nanoparticle imaging of pathological endothelium also offers a translational MRI strategy to identify human AVF prone to early failure.

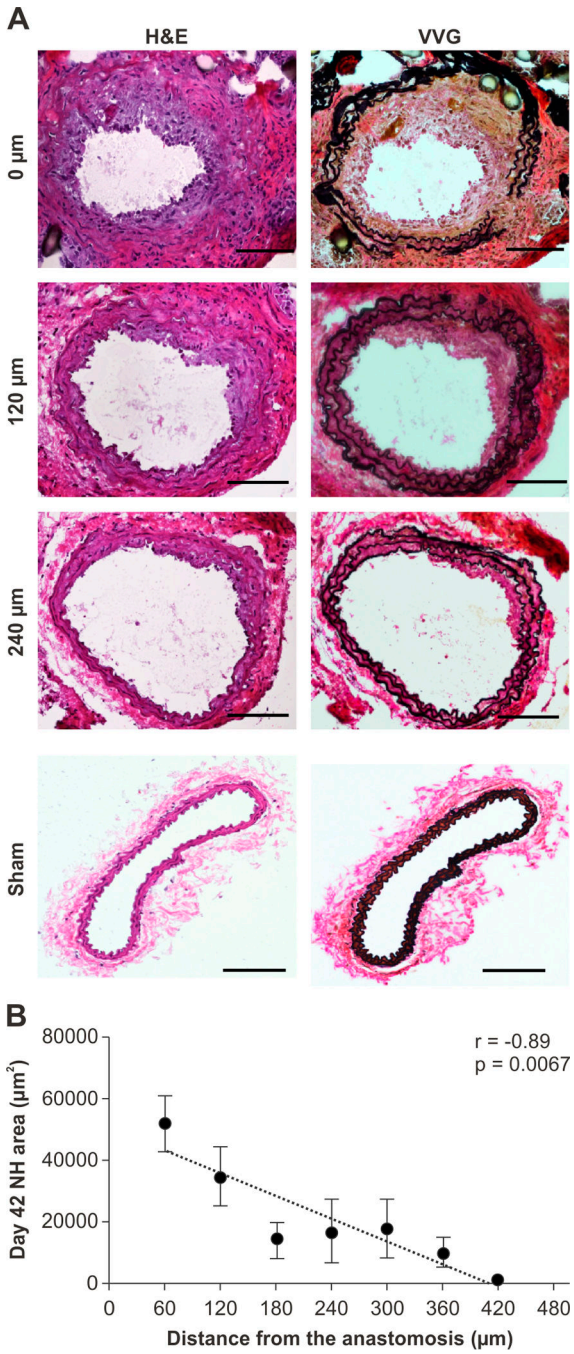

Figure 1.

Representative AVF pathology at day 42 after AVF creation. **A**. Neointimal hyperplasia was evident in the inflow arterial limb of the AVF (hematoxylin and eosin (H&E), left column; Van Gieson's stain (VVG), right column; Scale bar, 100 µm). **B**. Correlation between the neointimal area in day 42 AVF as a function of increasing distance from the anastomosis ($r = -0.89$, $p = 0.0067$, $n = 7$ mice). Error bar, S.E.M.

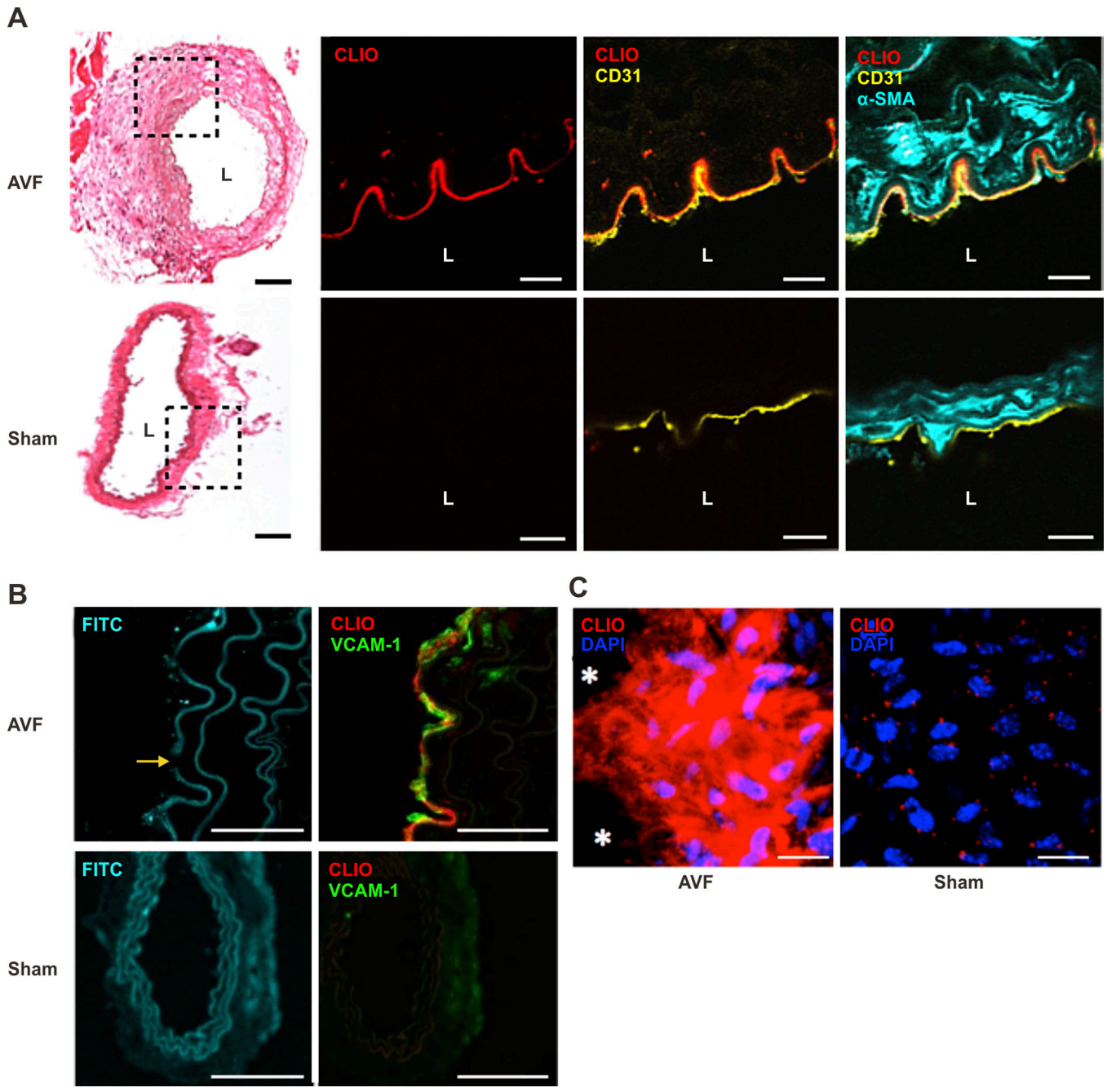

Figure 2.

CLIO-VT680 nanoparticle deposition in AVF intima. **A**. Hematoxylin and eosin (H&E) with NIR fluorescence microscopy of CLIO-VT680 deposition, and merged immunofluorescence images of day 14 AVF sections at 120 μm from the anastomosis (CD31, yellow; alpha-smooth muscle actin cells (αSMA), cyan; scale bar, 100 μm). CLIO-VT680 deposited in the AVF and colocalized primarily with CD31-positive endothelial cells. Minimal CLIO-VT680 uptake was present in sham-operated contralateral carotid arteries. Scale bar H&E, 100 μm; for fluorescence images, 25 μm. L=lumen. **B**. Fluorescence microscopy of fluorescein isothiocyanate (FITC)-channel autofluorescence

demonstrated medial cell layer expansion and an elastin break (yellow arrow) in the enlarged AVF arteries compared to sham-operated arteries. The endothelium of AVF expressed VCAM-1 (green) that localized with CLIO-VT680 (red). There was minimal VCAM-1 expression in sham-operated arteries. Scale bar, 25 μm. **C**. *En face* confocal microscopy showed CLIO-VT680 deposition in AVF tissues near the anastomosis, and minimal uptake in sham-operated contralateral carotid arteries. *indicates the anastomosis. Scale bar, 25 μm.

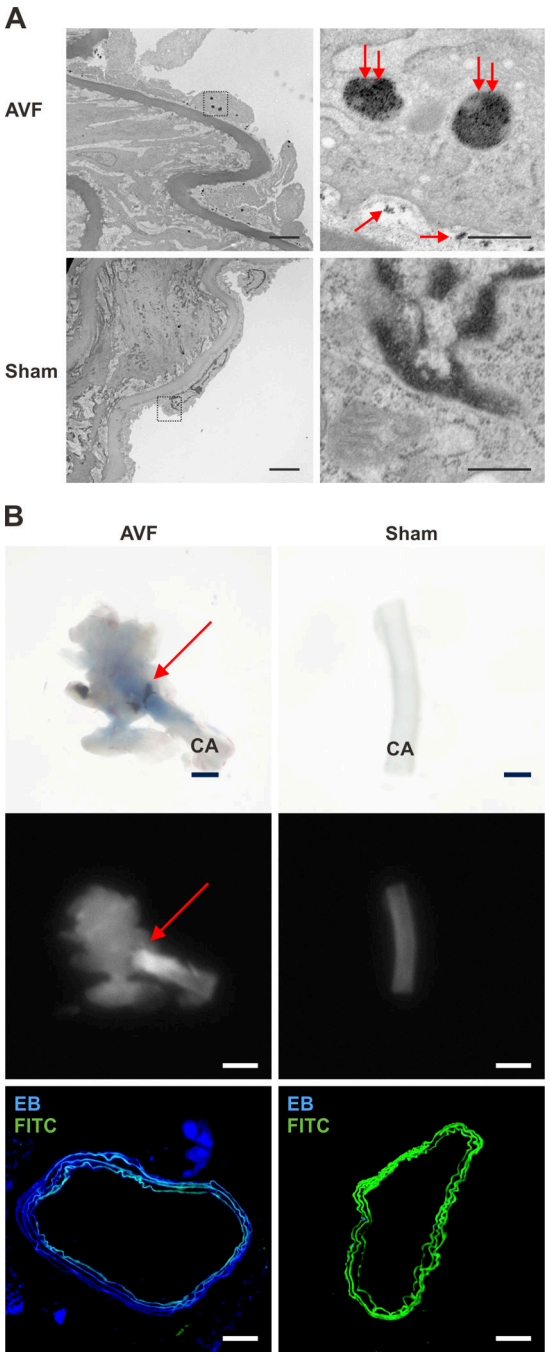

Figure 3.

Assessment of CLIO-VT680 nanoparticle localization within the arterial segment of AVF. **A**. Transmission electron micrographs of a representative day 14 CLIO-VT680 injected animal. In AVF, CLIO-VT680 nanoparticles (double red arrows, large nanoparticle clusters) were found inside the endothelial cells and between the endothelial cells and the basement membrane (single red arrows, smaller nanoparticle collections). There was minimal CLIO-VT680 particles deposition in sham-operated control arteries (lower row). Left column panel: scale bar, 4 μm. Right column panel: scale bar, 0.5 μm. IEL, internal elastic lamina.

B. Light microscopy (top row) and fluorescence reflectance imaging (middle column) of day 14 AVF showed Evans blue deposition in the juxta-anastomotic AVF zone, but only minimally in the sham-operated contralateral carotid artery (scale bar: 1 mm). Fluorescence microscopy (lower row) showed strong Evans blue signal (blue) in the AVF carotid arterial wall, with little signal in sham-operated contralateral arteries. Scale bar, 100 μm. CA, carotid artery, EB, Evans Blue, FITC, fluorescein isothiocyanate.

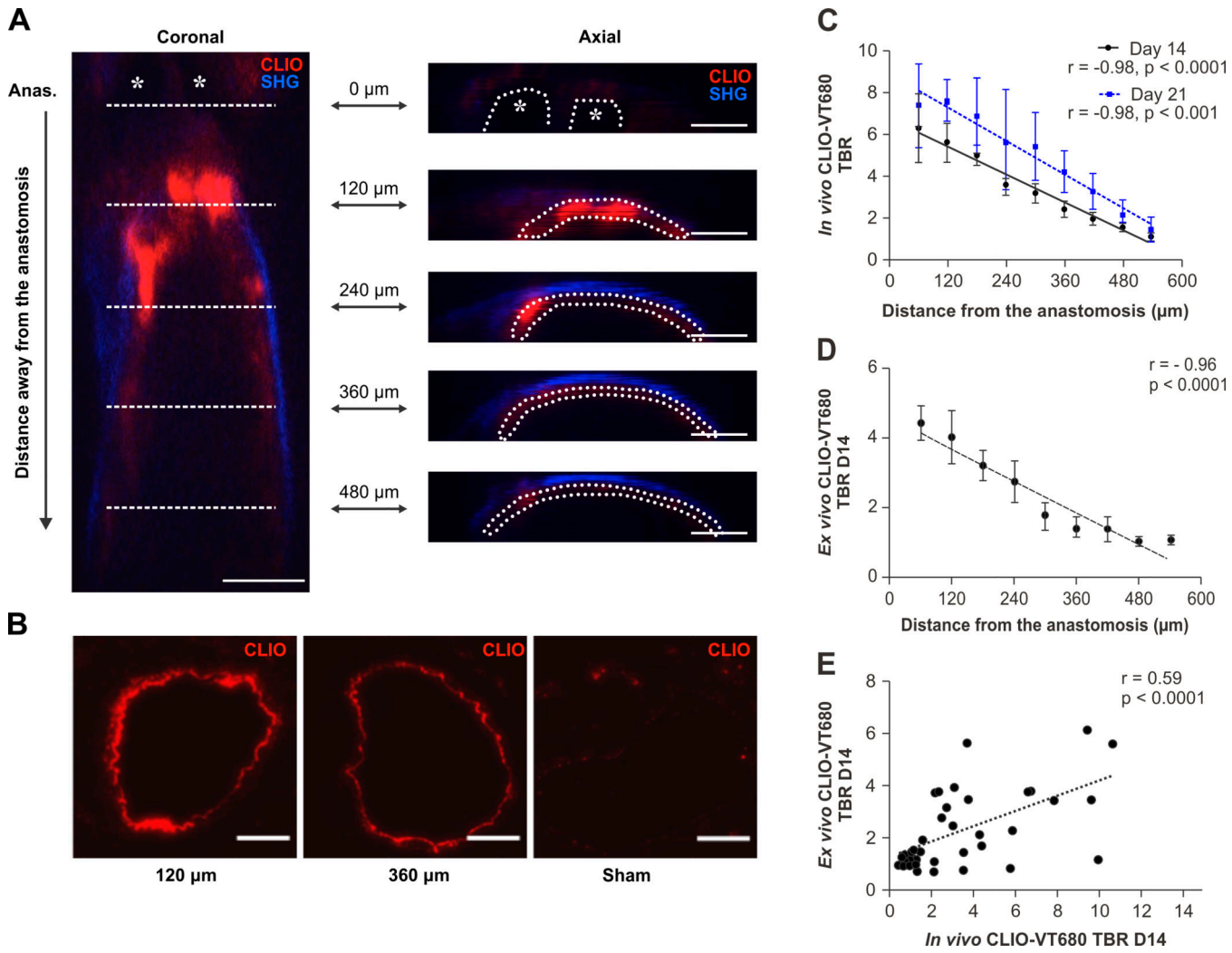

Figure 4.

Intravital microscopy (IVM) of CLIO-VT680-demarcated pathological endothelium in AVF. **A**. Coronal IVM image of a murine AVF. Asterisks indicate the sutures at the anastomotic site (ANAS). This point served as the reference point for analysis (0 µm mark) for each mouse. An axial AVF summation stack image (7 summed sections, comprising a 10µm thick section) was created at the anastomosis (0 µm), and then every 120 µm up to 480 µm away from the anastomosis. Axial scale bar, 100 µm. Red=CLIO-VT680 (pathological endothelium); blue=second harmonic generation signal from arterial wall collagen. IVM images were processed and windowed identically. **B**. Fluorescence microscopy images of CLIO-VT680 deposition in AVF sections 120 µm and 360 µm from the anastomosis, and the sham-operated contralateral side. Scale bar, 100 µm. **C**. The relationship between *in vivo* pathological endothelial signals (TBR) illuminated by CLIO-VT680 on day 14 and day 21 AVF as a function of the distance from the anastomosis. **D**. *Ex vivo* CLIO-VT680 signal in the AVF arterial segment measured by fluorescence microscopy as a function of the distance from the anastomosis (n=5 sections per point). **E**. Correlation between the CLIO-VT680

IVM signal and fluorescence microscopy signal. TBR, target-to-background ratio. Error bar, S.E.M.

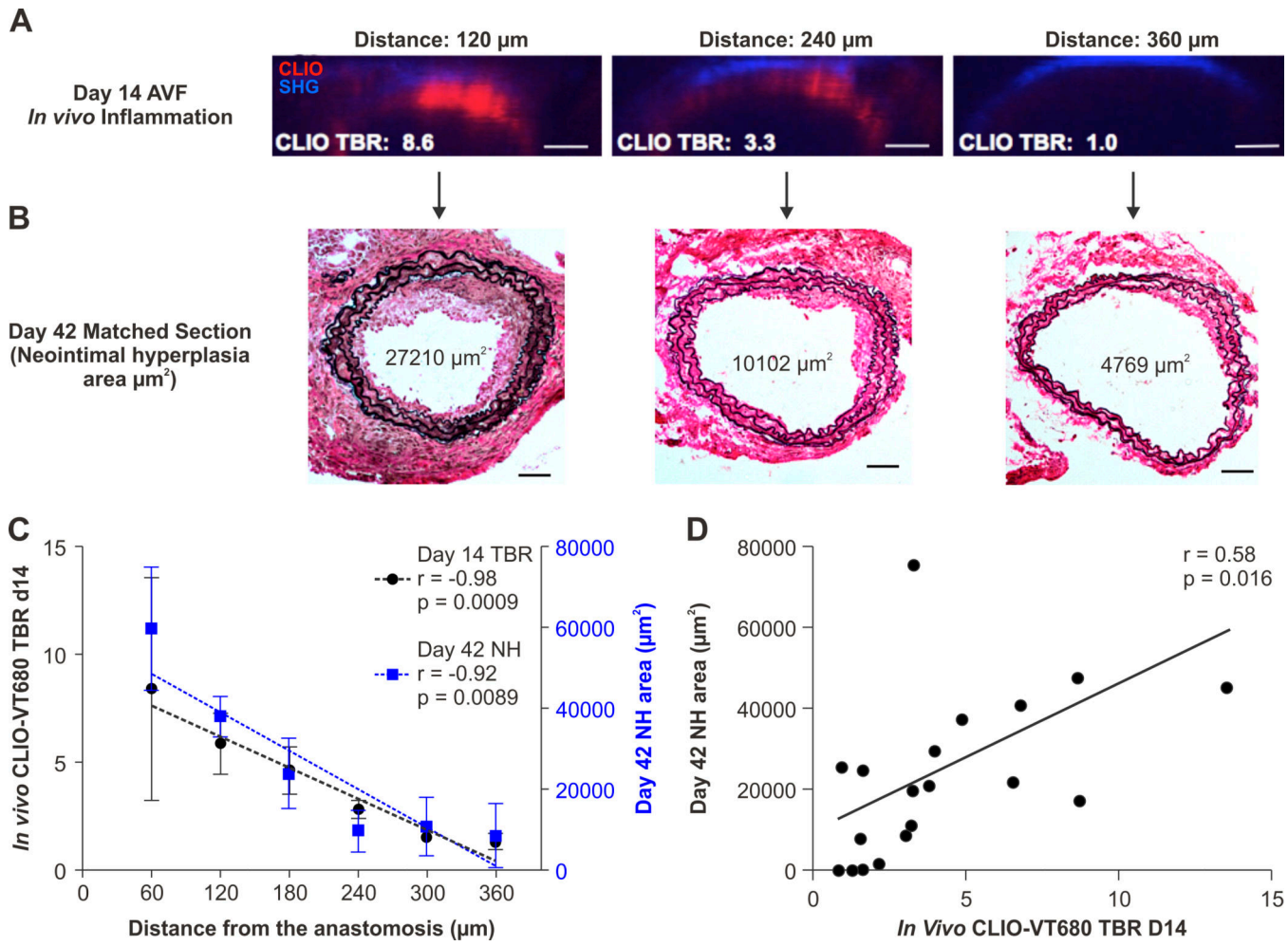

Figure 5.

Pathological endothelium *in vivo* and the development of subsequent AVF inflow stenosis. **A,B**. Representative day 14 survival IVM axial images and subsequent matched day 42 histological images. The anastomosis was identified by suture ligatures and served as the fiducial zero reference point for matching. Red=CLIO-VT680; Blue=second harmonic generation (SHG) signal. IVM images were processed and windowed identically. Scale bar, 50 µm. C. *In vivo* day 14 CLIO-VT680 TBR measured by IVM and day 42 neointimal hyperplasia in the arterial segment, as a function of the distance from the anastomosis. Error bar, S.E.M. **D**. Correlation between the *in vivo* IVM CLIO-VT680 signal at day 14 and the degree of subsequent neointimal hyperplasia at day 42 (17 AVF sections from 3 animals).

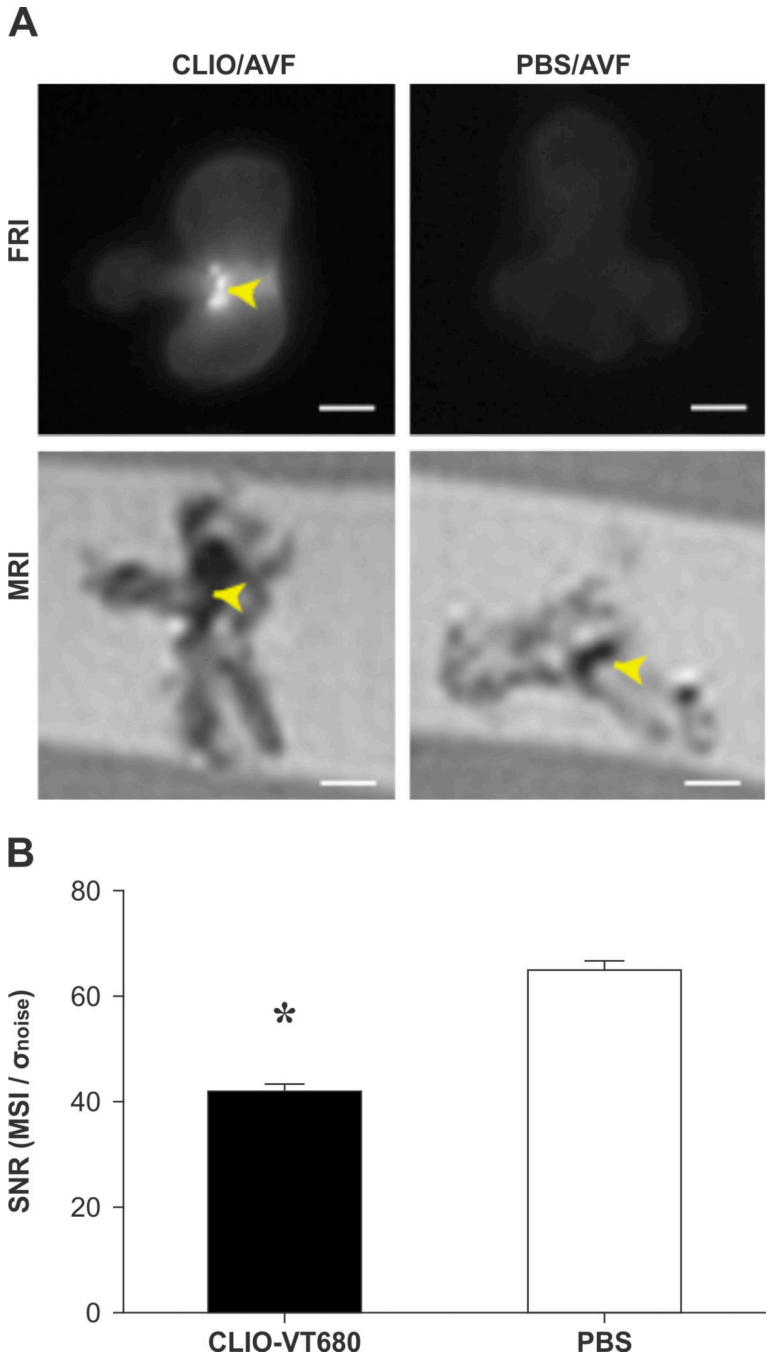

Figure 6.

Ex vivo molecular MRI of pathological endothelial signals using the CLIO-VT680 magnetofluorescent nanoparticle reporter. Day 14 AVF underwent *ex vivo* MRI twenty-four hours after injection of CLIO-VT680 (n=3) or control PBS (n=2). **A**. Fluorescence reflectance imaging (FRI) demonstrated strong focal NIRF signal enhancement (arrowhead) at the anastomosis in CLIO-VT680 injected animals (top row). In contrast, minimal fluorescence signal was noted in PBS-injected AVF tissues (right column). T2*-weighted rapid acquisition with relaxation enhancement (RARE) images by 7T MRI of the same,

respective AVF showed strong signal loss (arrowhead) in the arterial segment of CLIO-VT680 injected animals. In PBS-injected mice, MRI signal loss was more focal and restricted to the suture zone of the anastomosis. Scale bar, 1 mm. FRI and MRI images respectively processed and windowed identically. **B**. Signal-to-noise ratio analysis of the arterial segment adjacent to the anastomosis showed reduced signal-to-noise ratio in the CLIO-VT680 group compared to the PBS group (p=0.003, unpaired t-test).